Oxidation of Metals (2021) 95:409–425
https://doi.org/10.1007/s11085-021-10026-x

ORIGINAL PAPER

Mechanical and Corrosion Response of 316SS in Supercritical CO_2

Andrew Brittan[1,3] · Jacob Mahaffey[2] · David Adam[1] · Mark Anderson[1]

Received: 28 November 2020 / Revised: 9 March 2021 / Accepted: 16 March 2021 /
Published online: 14 May 2021

Abstract

The supercritical carbon dioxide (s-CO_2) Brayton cycle is currently being explored as a replacement for the steam Rankine cycle due to its potential for higher efficiency and lower cycle cost. 316 stainless steel is a candidate alloy for use in s-CO_2 up to roughly 600 °C, but the mechanical effects of prolonged exposure of base and welded material in s-CO_2 have not been analyzed. The potential for carburization makes this an important concern for the implementation of 316 and similar austenitic stainless steels in the s-CO_2 environment. In this study, welded and base material of two types of 316–316L and 316H–were exposed in either s-CO_2 or argon at 550 °C or 750 °C for 1000 h. 550 °C s-CO_2 exposure yielded a thin (< 1 μm) Cr oxide with occasional nodules of duplex Fe oxide and Fe–Cr spinel that were up to 5 microns thick. However, tensile results from s-CO_{-2} exposure matched those of 550 °C thermal aging in Ar, indicating that no mechanically detrimental carburization occurred in either 316 variant after 1000 h exposure. Conversely, 750 °C s-CO_2 exposure produced roughly 10 × the oxide thickness, with a more substantial Fe oxide (3–5 μm) on the majority of the surface and nodules of up to 40 μm thick. In comparison to aged samples, tensile testing of 750 °C CO_2-exposed samples revealed ductility loss attributed to carburization. Projections of 316L performance in s-CO_2 indicate that mechanically detrimental carburization—equal to that shown here for 750 °C, 1000 h—will likely be present after 7–14 years of service at 550 °C.

Keywords 316 Stainless Steel · Supercritical carbon dioxide · Mechanical properties · Oxidation · Carburization

✉ Andrew Brittan
andrewbrittan@hotmail.com

[1] University of Wisconsin-Madison, 1500 Engineering Drive, Madison, WI 53706, USA

[2] Sandia National Laboratory, 1611 Innovation Pkwy SE, Albuquerque, NM 87123, USA

[3] Present Address: Kairos Power, 707 W Tower Ave., Alameda, CA 94608, USA

Introduction

316 austenitic stainless steel (316) has proven to be very useful across a range of applications. It has shown similar or better oxidation resistance than comparable alloys (good up to roughly 600 °C), such as 347, 9Cr steel, or 12Cr steel [1–3], and has good strength up to 550 °C [4]. Additionally, 316 has been shown to have good ductility, machinability, and weldability, and is nuclear code certified in the USA [5]. It is currently used in many industrial applications and is being pursued for intermediate temperature components in developing fast breeder reactor designs [6–8] and other aspects of the nuclear industry [9, 10].

Furthermore, 316 is a candidate alloy for use in the supercritical carbon dioxide (s-CO_2) Brayton cycle, which is currently being considered for next generation power systems across several power sources. The Brayton cycle has the potential to produce higher efficiencies than the current industry standard, the Rankine cycle [11, 12]. Implementing an economically viable s-CO_2 Brayton cycle, however, requires a thorough understanding of the effects of the environment on the candidate materials [13]. Carbon corrosion is of particular interest, as the danger of forming Cr carbides brings the risk of decreased corrosion resistance and mechanical performance, especially in steels [5, 14–16].

Long-term exposure of materials at high temperature in s-CO_2 can affect material properties through two mechanisms: thermal aging and corrosion. Thermal aging of 316 has been shown to promote the formation of secondary phases and other precipitates, with the rate of growth and type of precipitate determined by the service temperature, time, and C content [17–19]. Higher C contents have been shown to produce increased carbides (Cr-rich, $M_{23}C_6$-type), while lower C has resulted in increased precipitation of intermetallics, such as the chi, sigma (σ), or laves phases. Of these intermetallics, σ-phase—$(Fe,Ni)_x(Cr,Mo)_y$—is of primary concern or this study because it is known to cause a loss of ductility and toughness below 120–150 °C [20–22]. While σ-phase is not apt to form in austenite, it forms very quickly in islands of delta-ferrite (δ-ferrite), which are known to be present within 316. In cases where carbide formation dominate, carbides develop along grain boundaries and create a depletion of Cr in the surrounding matrix, sensitizing the material and lowering the corrosion resistance of the nearby matrix [19, 23]. Cr-rich carbide growth occurs most quickly between 750 and 900 °C, though it also occurs more slowly at lower temperatures [24]. Therefore, both temperatures analyzed in this study, 550 °C and 750 °C, allow for carbide formation, and the precipitation at 750 °C should provide information on the long-term impact of carbides at 550 °C.

Corrosion of 316 and similar austenitic stainless steels in s-CO_2 has been primarily analyzed in terms of oxide analysis. This oxidation has been shown to be very minimal at temperatures of up to roughly 600 °C [1–3], above which it exhibits spallation and possible breakaway oxidation. At 550 °C, for example, it has performed only slightly worse than Ni-based superalloys (such as INCONEL 625) in terms of mass change and oxide thickness [1, 25, 26]. Under these conditions for 1000 h, it has shown to form a primary, thin Cr_2O_3 scale with occasional nodules of duplex oxide including an outer magnetite (Fe_3O_4) and an inner, more protective Fe–Cr

spinel. The size and density of the duplex oxide regions are important, as they have been correlated with carburization in Fe-based alloys [14, 27]. Corrosion in supercritical water has generally been found to be more aggressive and forms a consistent duplex oxide at as low as 400 °C after 250 h [28, 29]. However, the potential impact of carbon deposition has not been thoroughly analyzed in current literature, and this represents a major knowledge gap in projecting 316 material performance over a 20-year life cycle of an s-CO_2 Brayton power cycle.

Additionally, a major structural concern when welding austenitic steels is the susceptibility to hot cracking [30, 31]. The composition of 316 is characterized by roughly 5% ferrite [5], and this provides resistance to hot cracking because it dissolves the elements that are harmful in austenite (S, B, and P) [30, 32]. After welding, ferrite forms primarily along the dendritic axes (with a vermicular or lathy shape), as well as in interdendritic regions (roundish in shape). Finally, it has been shown that the fusion zone of 316L is the weakest part of a weld joint [33].

The potential degradation of mechanical properties due to carbon ingress—especially at the weld—for 316 after exposure in s-CO_2 was the motivation for the study that is presented here.

Experimental Procedures

Material compositions for the 316 used in this work are given in Table 1, with manufacturer composition ranges provided for the filler metals. All base material used was annealed, and no post-weld heat treatment was applied. Welded samples were created through manual gas tungsten arc welding of 3.18-mm plates using the parameters listed in Table 2. Welded plates were then milled from both sides to 1.59 mm thickness to remove surface effects. Samples were cut transgranularly from the welded plates using electrical discharge machining (EDM) so that the gauge of tensile samples incorporated each of base material, heat-affected zone (HAZ), and fused material, see Fig. 1. Tensile samples were designed in compliance with the ASTM standard E8/E8M Sect. 6.3 [34], with a slight elongation of the gauge to incorporate a maximum amount of the weld. Ellipsoidal corrosion samples were cut in the region between the gauges of neighboring tensile samples. This resulted in a variation in the amount of fused material in each sample, so sample mass change was not used as a quantitative indicator of the influence of welding of corrosion rate. It should be noted that the geometry of all welded samples are similar to those shown in Fig. 1. Base material samples of 316L were produced from 3.18 mm plate which was machined to 1.59 mm thickness before being EDM cut, including the ellipsoidal corrosion samples. 316H base corrosion samples were EDM sliced to dimensions of $16.8 \times 12.7 \times 1.59$ mm out of 12.7 mm bar stock. A separate exposure was performed with 316L corrosion samples from a different heat cut into square samples (described previously [35, 36], with dimensions of $12.7 \times 12.7 \times 1.59$ mm) in order to show repeatability and time dependence. All samples contained a 3.18-mm-diameter hole to allow for suspension from an alumina rod during exposure, except for the ellipsoidal corrosion samples, which had a 0.79-mm-diameter

Table 1 Composition of 316 base and filler material used in this work (wt. %)

	Cr	C	Mn	Mo	Si	P	S	Ni	N	Fe
316L (base)	16.73	0.019	1.22	2.07	0.39	0.03	0.0036	10.07	0.030	Bal
316H (base)	16.07	0.0523	0.840	2.09	0.504	0.0272	–	10.08	–	Bal
316L (filler)	18–20	0.03	1.0–2.5	2.0–3.0	0.30–0.65	Max 0.03	Max 0.03	11.0–14.0	–	Bal
ER316H (filler)	18–20	0.04–0.06	1.0–2.5	2.0–3.0	0.30–0.65	Max 0.03	Max 0.03	11.0–14.0	–	Bal
316L (square)	17.09	0.03	1.56	2.01	0.29	0.032	< 0.001	10.12	0.050	Bal

Table 2 Welding parameters

	316L	316H
Filler metal wire diameter (imm)	3.18	2.38
Shielding gas	Ar	Ar
Root gap (mm)	3.18	3.81
Joint type	Square butt	Square butt
Number of passes	1	1
Weld current (A)	125	141
Travel speed (mm/min)	50–75	50–75

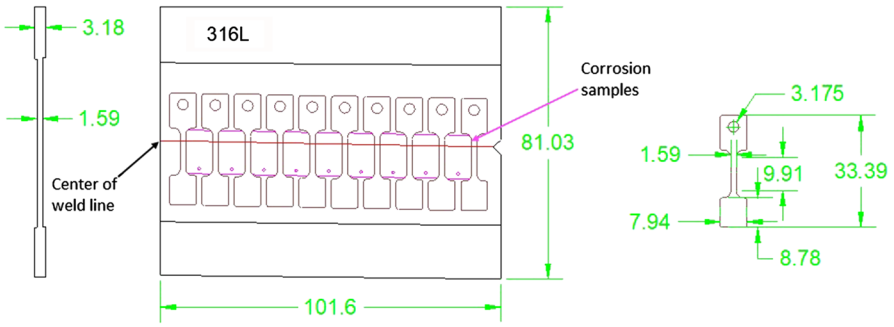

Fig. 1 Diagram showing where specimens were removed from a machined, welded plate, along with tensile specimen dimensions (dimensions in mm)

hole and were suspended using Ni wire. Samples were polished to 800-grit using SiC polishing paper prior to either exposure or tensile testing.

The exposure facility utilized in this experiment has been described in previous publications [1, 35, 37]. Continual exposures of 1000 h were performed in two different environmental compositions at each of 550 °C and 750 °C: research grade s-CO_2 (99.999% pure) at 20 MPa or ultra-high-purity Ar (99.999% pure) at 0.12 MPa. Included in each of these exposures were tensile and corrosion samples. Welded and base samples of both 316L and 316H were included in all exposures, with the exception of the 750 °C s-CO_2 exposure which contained only 316L. An additional s-CO_2 exposure was performed at 550 °C for increments of 200 h and a total of 1000 h with the square corrosion samples of 316L. The total number of samples used for tensile and corrosion analysis are given in Table 3 (for time-dependent analysis, one sample was removed after every 200 h).

Mass measurements were made before and after all exposures using a high precision Sartorius scale with an accuracy of ± 2 µg. Samples were dimensioned using a Starrett No. 795 M digital micrometer with an accuracy of ± 1 µm for thickness and a digital camera in tandem with image processing for cross-sectional area, resulting in a total surface area measurement with an accuracy within 1%. Microhardness measurements were performed on samples polished to a final step of 0.02 µm colloidal silica, using a Buehler Micromett II microhardness tester. Testing was performed

Table 3 Total number of 316 samples tested at each analysis condition

Type of sample	As-received tensile	550 °C s-CO_2		750 °C s-CO_2		550 °C Ar		750 °C Ar	
		Corrosion	Tensile	Corrosion	Tensile	Corrosion	Tensile	Corrosion	Tensile
316L Base	2	1	5	1	2	2	2	2	2
316L Weld	4	2	3	2	2	2	3	2	2
316H Base	2	2	2	0		2	3	2	2
316H Weld	2	2	2			2	3	2	2
*316L Square	N/A	6	N/A						

All exposures for 1000 h except for 316L square samples, which were exposed in the time dependency test and one sample was removed every 200 h

according to the ASTM standard E92, using an average of 25 measurements per sample with the following settings: 50 gf load; 15 s dwell time; and spacing of at least 2.5 diagonal lengths between impact centers [38]. Tensile testing was performed at room temperature, and stress data were acquired from an MTS Criterion 43 with a 5kN load cell. Strain data were acquired from a custom video extensometer setup which was verified to an accuracy of 1.2% for the Young's Modulus and a median difference per tensile measurement of 3% relative to an off-the-self extensometer on larger samples. Samples were analyzed using a field emission scanning electron microscope (FE-SEM), which included measuring oxide thickness.

Results

Mass Change

Mass change for both 316 variants was measured for each s-CO_2 and aging exposure (the latter for quality assurance) and is shown in Table 4 (all consecutive

Table 4 Mass change after 1000 h exposures (mg cm^{-2})—316H base value appears lower due to including rectangular sample mass change

Type of sample	550 °C s-CO_2	750 °C s-CO_2	550 °C Ar	750 °C Ar
316L Base	0.520 ± 0.006	3.27 ± 0.09	− 0.013 ± 0.052	− 0.072 ± 0.054
316L Welded	0.337 ± 0.006	3.22 ± 0.36	0.003 ± 0.007	− 0.038 ± 0.003
316H Base	0.393 ± 0.219	N/A	− 0.002 ± 0.028	− 0.052 ± 0.055
316H Welded	0.313 ± 0.031		− 0.001 ± 0.006	− 0.031 ± 0.015

1000 h exposures) and Fig. 2 (all rectangular samples). Mass change showed a large dependence on sample geometry, with tensile samples (at 550 °C, 316H: 0.571 ± 0.019 mg cm^{-2}) exhibiting consistently higher mass change than rectangular corrosion samples (at 550 °C, 316H: 0.126 ± 0.015 mg cm^{-2}). Therefore, after accounting for geometry, 550 °C s-CO_2 exposure produced higher mass change in base material samples than in welded ones. This is especially interesting in the case of 316H, as sensitization during the welding process has been shown to decrease its corrosion resistance near grain boundaries, as discussed above. Time dependence was found using a power fit on the measurements from square 316L samples shown in Fig. 2. The result was plotted alongside the data in Fig. 2, and the equation is given in (1), where t is the exposure time at 550 °C in hours.

$$\text{mass change}\left[\frac{\text{mg}}{\text{cm}^2}\right] = 0.0046 \cdot t^{0.48} \tag{1}$$

The exposure at 750 °C, being a more extreme environment, resulted in an order of magnitude increase in mass gain. All samples, welded or base, experienced mass gain in the range of 2.94–3.73 mg cm^{-2} with the exception of a single sample of welded 316L which showed a mass loss of 1.21 mg/cm^2. This sample was the only one which exhibited spallation and, as such, it was omitted from aggregated statistics. Therefore, mass change shows that corrosion was roughly equivalent for both welded and base material at 750 °C in s-CO_2 for 1000 h. It is likely that any microstructural differences between base and welded material which caused differences in corrosion response at 550 °C were overwhelmed at 750 °C. It is anticipated that spallation would occur on all samples exposed to 750 °C CO_2 given additional thermal cycling.

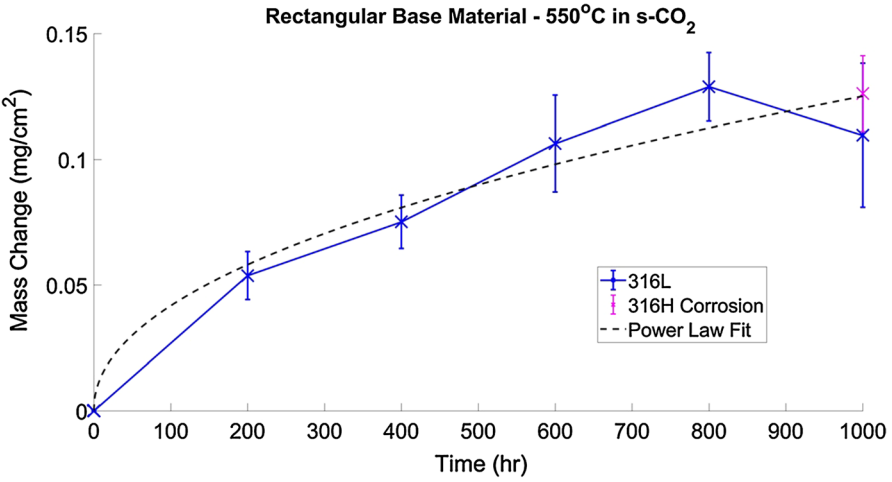

Fig. 2 Mass change for rectangular 316L and 316H after exposure in s-CO_2 at 550 °C, 20 MPa. 316L shows parabolic oxidation performance, and 316H produced equivalent mass change after 1000 h

Oxide Analysis

After s-CO_2 exposure at 550 °C, the surface of both 316 variants was dominated by a Cr-rich oxide. This oxide was very thin—on the order of 100 s of nanometers based on cross-sectional SEM—and protective. As the surface images in Fig. 3, there were also occasional nodules of dual-phase Fe-based oxide (point 2), which have been speculated to nucleate after the formation of the Cr-rich oxide (point 1) [39]. Cr was not present in the magnetite layer on the surface of the Fe oxide nodules. It was not possible to accurately analyze the thinner oxide due to the nature of EDS scans (penetrating into the base material, as observed by the high Ni signal in point 1 of Fig. 3).

The corrosion of 316 at 550 °C after 1000 h was very minor, matching that of previous work [1–3]. The oxide and near-surface region can be seen in Fig. 4 for both base and fusion regions. Figure 4 confirms that the majority of both regions was indeed covered by a thin (< 1 µm) Cr scale, and occasional nodules of Fe-rich oxide were observed to be up to 5 µm thick (see Fig. 4a). This represented a relatively small amount of total oxidation. Based on the theory that C is liberated through the oxidation process in the s-CO_2 environment [14, 27], it can be projected that very little C was deposited.

CO_2 corrosion of 316L at 750 °C was much more aggressive, with oxide thickness on the order of 10 times that of 550 °C, see Fig. 4c. The base oxide, composed of what appeared to be columnar, outward growing iron oxide (EDS showed no Cr) was observed to be 3–5 µm thick. Nodules of duplex oxide with an inner Fe–Cr spinel and outer Fe oxide were also present, see Fig. S1, with a maximum observed thickness of roughly 40 µm. The enhanced corrosion at the nodules was likely assisted by the voiding inherent in both layers of the duplex oxide (assisted in the Fe–Cr spinel by the deposition of C) [15, 27, 40]. Additionally, the internally

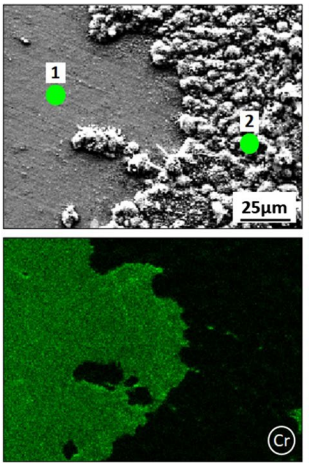

Element	Atomic %	
	Point 1	Point 2
Fe	47.7	61.5
Cr	14.9	1.6
O	25.1	33.0
Ni	7.5	0.3

Fig. 3 Surface EDS of 316L exposed at 550 °C, 20 MPa for 1000 h. Image includes two point scan locations, whose primary measured constituent values are given to the right

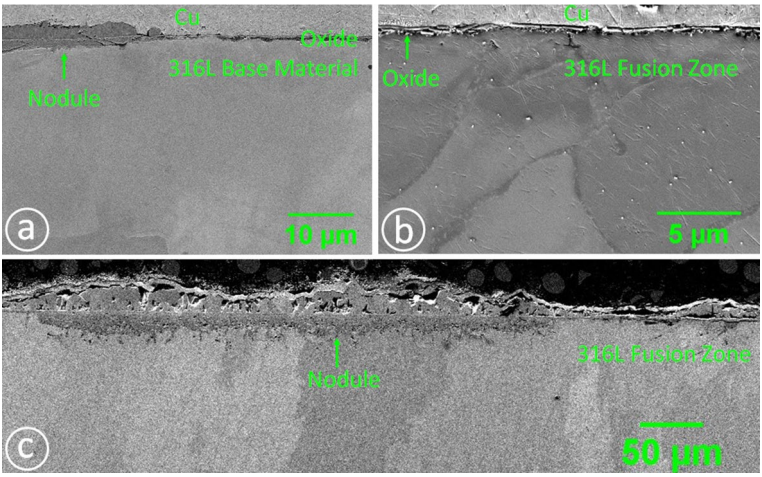

Fig. 4 **a**, **b**: Cross section image of 316L base **(a)** and fusion **(b)** material after exposure to s-CO_2 at 550 °C, 20 MPa for 1,000 h. Base material shows a thick nodule, while the majority of the surface (both base and fusion zones) resembles that shown in the fusion image. c: Cross section image of 316L fusion region after exposure to s-CO_2 at 750 °C, 20 MPa for 1000 h. Base and fusion zones both show a similar oxide morphology to that of 550 °C, but nodules and base oxide are much thicker

grown Fe–Cr spinel has been associated with carburization in s-CO_2 environments. The presence of a relatively large Fe–Cr spinel in the nodules formed at 750 °C (especially compared with those formed at 550 °C) indicates that carburization may affect mechanical properties in the form of near-surface carbide formation.

Fusion and base material regions were etched with Kalling's #2 in an attempt to reveal carburization, see Fig. 5, though it was somewhat inconclusive. Occasional carbide embrittlement is observed throughout the material (due to alloy C), and it is not visually obvious that this increases along the typical, single phase oxide pictured in base metal in Fig. 5b. The weld region is similar: precipitates were observed throughout, though there is a possible increase within about 20–40 microns of the duplex oxide nodules shown in Fig. 5a. This is representative of nodule performance both in the fusion zone and in base metal.

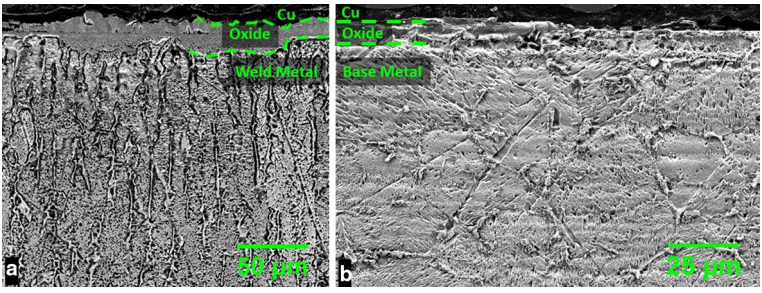

Fig. 5 Kalling's #2 etched surface of 316L exposed to CO_2 at 750 °C, 20 MPa for 1000 h of two different regions: **a** fusion zone and **b** base metal

Thermal Aging Analysis

Microhardness Testing

In order to better understand the effects of the microstructural changes in 316, microhardness measurements were performed on 316L base material before and after aging. Prior to exposure, the hardness of the 316L used in this experiment was found to be 188 ± 2 HV, well within the typical hardness for this material [41, 42]. Aging at 550 °C resulted in a very slight increase to 197 ± 2 HV. 750 °C aging, meanwhile, resulted in a more significant increase in hardness: 212 ± 3 HV. Both increases are indicative of an effect of thermal aging, likely due to the transformation of soft ferrite into harder precipitates: $M_{23}C_6$ carbides and intermetallic phases [18–20]. The larger increase after aging at a higher temperature is likely due to additional coarsening of these precipitates. The effect of this on tensile properties is expected to be mild, though a slight increase in yield strength would fit this effect.

Tensile Results

Tensile results for base material are given in Table 5. As expected from our analysis above, there was very little effect of either s-CO_2 exposure or aging at 550 °C for 1000 h. Results for 316L and 316H at this temperature, while differing slightly from each other in strength and ductility, either had overlapping uncertainty bands or else represented only minimal changes that cannot be used to draw any definite conclusions. However, both 316L and 316H were mechanically altered after both exposures at 750 °C for 1000 h. In both alloys, thermal aging lowered yield strength (YS) and elongation, and in 316H it led to an increased ultimate tensile strength (UTS). The most striking difference between aging and s-CO_2 exposure in 316L was the severe drop in elongation associated with s-CO_2 exposure.

The results for welded samples are listed in Table 6. For 316L, both exposures at 550 °C increased UTS, while having little total effect on yield strength or elongation. For 316H, 550 °C had an overall minimal effect, similar to that of base material.

Table 5 Tensile results for base material samples after the given exposure [43] (* = values previously published [44])

	UTS (MPa)	0.2% YS (MPa)	Elongation (%)
*316L: As-received	624 ± 7	302 ± 2	76.1 ± 0.7
316L: 550 °C s-CO_2	627 ± 14	296 ± 6	74.8 ± 1.3
*316L: 750 °C s-CO_2	598 ± 11	220 ± 1	26.6 ± 3.3
316L: 550 °C Aging	635 ± 3	305 ± 2	73.6 ± 0.6
*316L: 750 °C Aging	630 ± 12	244 ± 4	60.9 ± 0.9
*316H: As-received	574 ± 1	274 ± 3	92.2 ± 1.0
316H: 550 °C s-CO_2	575 ± 2	282 ± 2	87.1 ± 5.9
316H: 550 °C Aging	579 ± 1	270 ± 1	83.6 ± 2.3
*316H: 750 °C Aging	617 ± 2	243 ± 1	67.6 ± 1.3

Table 6 Tensile results for transverse welded samples after the given exposure

	UTS (MPa)	0.2% YS (MPa)	Elongation (%)	Failure location
316L: As-welded	539 ± 6	270 ± 7	41.1 ± 0.9	Fusion zone
316L: 550 °C s-CO_2	592 ± 4	294 ± 8	40.0 ± 0.9	
316L: 750 °C s-CO_2	586 ± 8	240 ± 9	19.2 ± 0.3	
316L: 550 °C Aging	560 ± 3	276 ± 4	36.2 ± 0.9	
316L: 750 °C Aging	627 ± 2	241 ± 2	40.1 ± 2.5	
316H: As-welded	583 ± 10	303 ± 1	49.0 ± 2.0	
316H: 550 °C s-CO_2	598 ± 5	291 ± 3	41.6 ± 0.8	
316H: 550 °C Aging	570 ± 11	278 ± 6	34.3 ± 3.8	
316H: 750 °C Aging	648 ± 4	260 ± 2	40.0 ± 2.9	

Also similar to base material, aging for both 316L and 316H at 750 °C lowered yield strength while increasing UTS. s-CO_2 exposure of 316L at 750 °C resulted in decreased YS and elongation, while there was an increase in UTS. However, relative to 750 °C aging, s-CO_2 corrosion of both welded and base material appears to have decreased both UTS and elongation considerably. As metal loss to oxidation was not considerable, the drop in elongation was likely due to carburization. The drop in ductility caused premature rupture during tensile testing, consequently lowering UTS. All samples ruptured in the fusion zone.

Fracture Surface Analysis

Analysis of the fracture surfaces of as-received base material of both 316L and 316H provides the baseline for ductility. The fracture surfaces, shown in Fig. 6a and b (316L) and Fig. 6e and f (316H), exhibit high ductility in the form of localized necking before fracture, as well as a transgranular fracture mode. Further, Fig. 6b

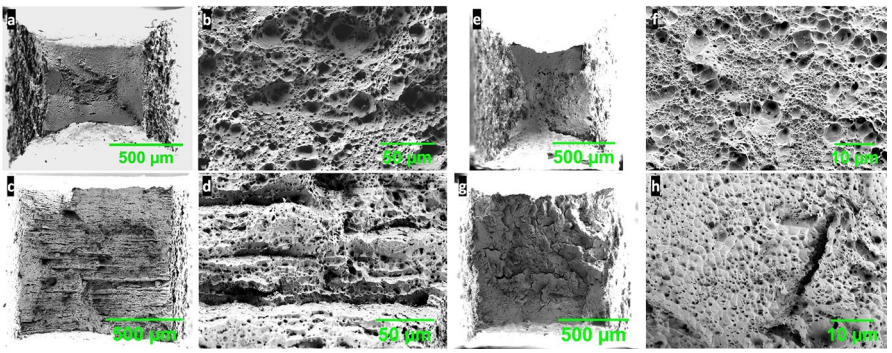

Fig. 6 Fracture surface images of base samples pulled in the as-received (316L: **a**, **b**; 316H: **e**, **f**) and 750 °C aged (316L: **c**, **d**; 316H: **g**, **h**) conditions. Loss of ductility after aging observed in lack of necking and decrease in dimple size, as well as horizontal striations (316L) and intergranular embrittlement and fracture (316H)

and f shows that micro-void coalescence (MVC) characterized these fractures, with large dimples: 5–25 μm for 316L, 1–10 μm for 316H. This was a very ductile fracture surface which correlated to the high elongation measurements.

After aging at 750 °C, 0.12 MPa for 1,000 h, both materials exhibited ductility loss in the form of decreased localized necking and reduced dimple size. Figure 6 c and d shows that 316L maintained transgranular fracture, but horizontal striations were observed on the fracture surface. These striations were likely due to the ferrite inclusions present in the rolled 316L plate from which samples were taken (and match the lamellae observed in Fig. S3). After aging at 750 °C, these inclusions were likely nearly completely transformed into intermetallics, likely dominated by σ-phase, along with some small percentage of carbides. Conversely, Fig. 6e and f shows that the extra C present in 316H caused grain boundary embrittlement and intergranular fracture after aging for 1000 h, likely due to the formation of Cr-rich $M_{23}C_6$ carbides (as observed in the Cr-enrichment in Fig. S4). This is consistent with previous work which showed that increased C content in 316 increases the precipitation of grain boundary carbides, while decreasing the precipitation of intermetallic phases such as σ-phase [45]. As discussed earlier, σ-phase is only embrittling below 120–150 °C, so it is likely to be the limiting factor in the material's ductility at room temperature, but not at high temperature. Carbide embrittlement, meanwhile, will be present at both high and low temperatures. Therefore, aging at 750 °C for 1000 h likely had very little-to-no degrading mechanical effect on 316L, but decreased ductility somewhat in 316H due to the increased C content.

The effect of s-CO_2 corrosion at 750 °C on the fracture mechanism, seen in Fig. 7, was to further limit ductility. The fracture surface exhibited no necking, and the center of the sample (shown in Fig. 7c) consisted of transgranular fracture with MVC. The edges of the sample, however, showed a combined transgranular and intergranular fracture, see Fig. 7b, evidence of moderate carbide embrittlement along grain boundaries. The depth dependence of this phenomena indicates that this was due to carburization from the environment. Additional exposure is anticipated to coarsen carbides as well as increase the depth of C penetration, both of which would further reduce sample ductility.

The appearance of the fracture surfaces of welded samples (see Figs. S8 and S9) was somewhat different due to the altered microstructure of the fusion zone.

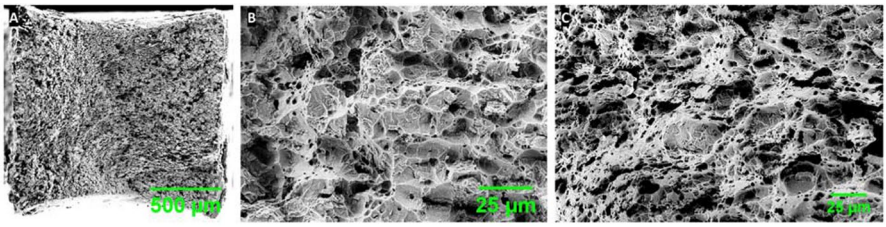

Fig. 7 Fracture surface images of base 316L pulled after exposure in s-CO_2 at 750 °C, 20 MPa for 1000 h (**a**: full surface; **b**: zoomed to show combined transgranular and intergranular cracking near the edge; and **c**: zoomed to show transgranular fracture with MVC in the center). Loss of ductility observed in lack of necking

However, they evolved in much similar ways to that of base material for each of 316L and 316H. For example, as discussed above, δ-ferrite forms in vermicular or lathy shapes along the axes of dendrites during weld re-solidification. Therefore, there was still σ-phase embrittlement in 316L welded samples, but it was oriented along the direction of the weld path instead of the rolling of the plate. The results support the above indications that the weld performed similarly to the base material in the s-CO_2 environment.

A comparison of tensile results showed little or no difference between the two exposures at 550 °C, and this was reflected in their fracture surfaces, analyzed with figures in Supplemental Information.

Discussion

This work further supports previous reports on the sensitivity of mechanical properties that alloy 316 has in the presence of free C at high temperatures. Results from aging show that the increased C in 316H reduces high-temperature ductility through the formation of grain boundary carbides (likely $M_{23}C_6$). It is, therefore, important to restrict carburization in 316L during contact with the s-CO_2 environment.

316L was able to form a protective scale in both base and fusion zones at 550 °C, a thin layer of Cr_2O_3 which covered nearly the entire sample surface. With the exception of a few small nodules, this scale protected against the formation of a duplex oxide which has been linked to carburization in s-CO_2. Consequently, there was no trend of observable effects of corrosion on the mechanical response of either 316L or 316H after exposure to s-CO_2 at 550 °C, 20 MPa for 1000 h. This result was consistent with welded samples as well, as there was no effect of weld sensitization observed. Exposed 316L welded samples did show an increase in UTS (and possible increase in YS), likely from the transformation of δ-ferrite into the σ-phase [20]. Exposure data for both base and welded samples shows some slight scatter which could be due in part to the presence of scattered surface oxide nodules. While it should be noted that the nodules of oxide are likely to grow—in both depth and width—from further exposure, it is not defined what effect continued exposure will have on the mechanical response of 316L. To better understand this, exposure at 750 °C was analyzed as a possible prediction of long-term exposure at 550 °C.

316L exhibited some mechanical degradation as a result of enhanced corrosion after s-CO_2 exposure at 750 °C, 20 MPa for 1000 h. Welded and base material responded similarly to each other after each exposure condition. Oxidation proved to be roughly an order of magnitude higher than that at 550 °C, with oxide nodules forming potential sites for stress concentration and crack initiation. Correspondingly, grain boundary embrittlement was observed near the oxide–metal interface, likely due to environment-induced carbide formation. The decreased ductility was reflected in the tensile results, which revealed a sharp drop in elongation for s-CO_2-exposed samples relative to neutral aging. This performance was consistent with both welded and base material, and there was no additional observed attack in either the HAZ or fusion zone. Aging of 316H at 750 °C resulted in a roughly 25% drop in ductility, attributable to intergranular carbide formation, but the effect was less than

the roughly 60% ductility loss from s-CO_2 corrosion of 316L. This further indicates the potential for mechanical failure of 316 in s-CO_2 if applied in a highly carburizing environment.

As the alloying C in both 316L and 316H is much greater than the matrix solubility [45], the long-term aging of either variant will result in precipitation of carbides with the majority of alloying C. Despite this, tensile results of both 550 °C and 750 °C aging experiments showed that carbides did not become ductility limiting in 316L in the absence of environmental carburization. Therefore, when considering the performance of 316L at 550 °C in s-CO_2, environmental carburization over long time scales presents the greatest threat to mechanical stability. Since 750 °C s-CO_2 exposure resulted in significant and quantified environment-induced ductility loss, this is used as reference point for a concerning level of corrosion. Roughly 7–10 × as much corrosion occurred in s-CO_2 at 750 °C than at 550 °C, based on the mass change and oxide thickness measurements. According to the time dependence section of this work, the parabolic kinetics defined in Eq. (1) shows that corrosion at 550 °C should increase to this level after 7–14 years. It is not clear whether this means that the level of carburization seen after 1000 h exposure at 750 °C will occur as a result of this corrosion in 550 °C environments, but the possibility of gradual, near-surface embrittlement should be a concern and be designed into pressure vessel components. Additionally, the deposition of carbon and formation of intergranular carbides occurring under creep or fatigue stresses is a potential source for crack initiation and likely a catalyst for faster propagation than previously observed in non-carbon containing environments [46].

Conclusions

This experiment was designed to analyze the effect of C on the performance of the 316 alloy in the s-CO_2 environment. This not only involved long-term aging of base material, but also the exposure to s-CO_2 at and above the upper temperature limit for 316 application in an s-CO_2 Brayton cycle, the higher temperature allowing for analysis of accelerated corrosion. In addition, both 316L and 316H were welded using GTAW and analyzed in the same environments. In this way, the study covered the potential implications of sensitization and higher alloying C on the performance of 316 in the s-CO_2 environment.

Conclusions from this work include:

- GTAW had no observed impact on the response of 316L or 316H to s-CO_2 exposure.
- After exposure to s-CO_2 at 550 °C for 1000 h, 316L exhibited no ductility loss due to carburization. Material ductility was limited by σ-phase precipitation which is not a concern above 150 °C.
- After exposure to s-CO_2 at 750 °C for 1000 h, 316L exhibited significant ductility loss due to carburization. Fracture mode switched from transgranular to intergranular due to environmental C ingress and carbide formation.

- After exposure for 1000 h to s-CO_2 at 750 °C, 316L exhibited less ductility in near-surface regions, where C buildup and carbide formation are likely highest. These regions could serve as crack initiation sites.
- The time dependence of 316L corrosion from s-CO_{-2} at 550 °C indicates that the total mass change (absent spallation) will equal that shown here for 750 °C, 1000 h after 7–14 years, well within a 20-year lifespan of an s-CO_2 Brayton power cycle. There is, therefore, a large concern for C-induced intergranular crack initiation and propagation in 316L at 550 °C, especially in the regions beneath duplex oxide formation.

Supplementary Information The online version contains supplementary material available at https://doi.org/10.1007/s11085-021-10026-x.

Acknowledgements The author gratefully acknowledges the contributions to the work made by Paul Brooks of the University of Wisconsin-Madison. Additionally, a special thanks to Ryan Carroll and Peter Li who performed significant work in completing this research. The author also acknowledges the assistance of Dr. Julie Tucker at Oregon State University for aiding the writing process of this research. Sandia National Laboratories is a multimission laboratory managed and operated by National Technology & Engineering Solutions of Sandia, LLC, a wholly owned subsidiary of Honeywell International Inc., for the U.S. Department of Energy's National Nuclear Security Administration under contract DE-NA0003525. This paper describes objective technical results and analysis. Any subjective views or opinions that might be expressed in the paper do not necessarily represent the views of the U.S. Department of Energy or the United States Government.

Funding This work was supported by Advance supercritical carbon dioxide cycles DE-EE0007120 and the U.S. Department of Energy.

Data Availability The data are available upon request from AMB.

Declarations

Conflict of interest The authors declare that they have no competing interests.

References

1. J. T. Mahaffey, "Effect of Partial Pressure of Oxygen and Activity of Carbon on the Corrosion of High Temperature Alloys in s-CO2 Environments," University of Wisconsin-Madison, 2017.
2. T. Furukawa, Y. Inagaki, and M. Aritomi, *Journal of Power and Energy Systems* **4**, (1), 2010 (252–261).
3. G. Cao, V. Firouzdor, K. Sridharan, M. Anderson, and T. R. Allen, *Corrosion Science* **60**, 2012 (246–255).
4. "Boiler and Pressure Vessel Code: Section II Part D." The American Society of Mechanical Engineers, New York, pp. 6–340, 2013.
5. S. Kou, *Welding Metallurgy*, (Wiley, New York, 2003).
6. S. L. Mannan, S. C. Chetal, B. Raj, and S. B. Bhoje, *Transactions of the Institute of Metal Finishing* **56**, (2), 2003 (155–178).
7. H. Lee, *Nuclear Engineering and Design* **308**, 2016 (142–153).
8. P. Kumar and A. Pai, *Procedia Engineering* **86**, 2014 (173–183).
9. A. Fissolo, B. Marini, G. Nais, and P. Wident, *Journal of Nuclear Materials* **233**, 1996 (156–161).

10. G. Zheng, B. Kelleher, G. Cao, M. Anderson, T. Allen, and K. Sridharan, *Journal of Nuclear Materials* **461**, 2015 (143–150).
11. V. Dostal, "A Supercritical Carbon Dioxide Cycle for Next Generation Nuclear Reactors," Massachusetts Institute of Technology, 2004.
12. Y. Kato, T. Nitawaki, and Y. Muto, *Nuclear Engineering and Design* **230**, (1–3), 2004 (195–207).
13. I. G. Wright, B. A. Pint, J. P. Shingledecker, and D. Thimsen, "Materials Considerations for Supercritical CO2 Turbine Cycles," in *ASME Turbo Expo 2013: Turbine Technical Conference and Exposition*, 2013.
14. D. Young, P. Huczkowski, T. Olszewski, T. Hüttel, L. Singheiser, and W. J. Quadakkers, *Corrosion Science* **88**, 2014 (161–169).
15. F. Rouillard, G. Moine, M. Tabarant, and J. C. Ruiz, "Corrosion of 9Cr Steel in CO2 at Intermediate Temperature II: Mechanism of Carburization," *Oxid. Met.*, pp. 57–70, 2012.
16. K. Arioka, T. Yamada, T. Terachi, and G. Chiba, *Corrosion Science* **62**, (7), 2006 (568–575).
17. V. Magula, J. Liao, K. Ikeuchi, T. Kuroda, Y. Kikuchi, and F. Matsuda, *Transactions of JWRI* **25**, (1), 1996 (49–58).
18. H. Shaikh, H. S. Khatak, S. K. Seshadri, J. B. Gnanamoorthy, and P. Rodriguez, "Effect of ferrite transformation on the tensile and stress corrosion properties of type 316 L stainless steel weld metal thermally aged at 873K," vol. 26, no. 7, pp. 1859–1868, 1995.
19. B. Weiss and R. Stickler, *Metallurgical and Materials Transactions* **3**, (April), 1972 (851–866).
20. T. P. S. Gill, M. Vijayalakshmi, J. B. Gnanamoorthy, and K. A. Padmanabhan, *Welding Journal* **65**, (5), 1986 (122–128).
21. C. Hsieh and W. Wu, *ISRN Metall.* **2012**, (4), 2012 (1–16).
22. D. M. E. Villanueva, F. C. P. Junior, R. L. Plaut, and A. F. Padilha, *Materials Science and Technology* **22**, (9), 2006 (1098–1104).
23. A. S. Lima, A. M. Nascimento, H. F. G. Abreu, and P. de Lima-Neto, *Journal of Materials Science* **40**, (1), 2005 (139–144).
24. J. W. Simmons, D. G. Atteridge, and S. M. Bruemmer, *Corrosion* **48**, (12), 1992 (976–982).
25. J. D. Tucker *et al.*, "Supercritical CO2 round robin test program," in *The 6th International Supercritical CO2 Power Cycles Symposium*, 2018.
26. J. D. Tucker, "Advancement of supercritical carbon dioxide technology through round robin testing and fundamental modeling," 2019.
27. F. Rouillard and T. Furukawa, *Corrosion Science* **105**, (April), 2016 (120–132).
28. M. Sun, X. Wu, Z. Zhang, and E. Han, *Corrosion Science* **51**, (5), 2009 (1069–1072).
29. K. I. Choudhry, S. Mahboubi, G. A. Botton, J. R. Kish, and I. M. Svishchev, *Corrosion Science* **100**, 2015 (222–230).
30. Y. Cui and C. D. Lundin, *Materials & Design* **28**, (1), 2007 (324–328).
31. T. W. Nelson, J. C. Lippold, W. Lin, and W. A. Baeslack III., *Welding Reasearch Supplement* **76**, (3), 1997 (110–119).
32. M. J. Cieslak, A. M. Ritter, and W. F. Savage, *Welding Journal* **61**, (January), 1982 (1–8).
33. R. M. Molak, K. Paradowski, T. Brynk, L. Ciupinski, Z. Pakiela, and K. J. Kurzydlowski, *International Journal of Pressure Vessels and Piping* **86**, (1), 2009 (43–47).
34. *ASTM E8/E8M-16a Standard Test Methods for Tension Testing of Metallic Materials*. West Conshohocken, PA: ASTM International, 2016.
35. J. Mahaffey, D. Adam, A. Brittan, M. Anderson, and K. Sridharan, *Oxidation of Metals* **86**, (5–6), 2016 (567–580).
36. J. Mahaffey, A. Schroeder, D. Adam, A. Brittan, M. Anderson, A. Couet, and K. Sridharan, *Metallurgical and Materials Transactions A* **49**, 2018 (1–12).
37. J. Mahaffey *et al.*, "Effect of Oxygen Impurity on Corrosion in Supercritical CO2 Environments," in *The 5th International Supercritical CO2 Power Cycles Symposium*, 2016.
38. *ASTM E92–17 Standard Test Methods for Vickers Hardness and Knoop Hardness of Metallic Materials*. West Conshohocken, PA: ASTM International, 2017.
39. T. D. Nguyen, J. Zhang, and D. J. Young, *Corrosion Science* **112**, 2016 (110–127).
40. F. Rouillard, G. Moine, L. Martinelli, and J. C. Ruiz, *Oxidation of Metals* **77**, (1–2), 2012 (27–55).
41. S. Adachi and N. Ueda, *Advanced Powder Technology* **24**, (5), 2013 (818–823).
42. S. Kalainathan, S. Sathyajith, and S. Swaroop, *Optics and Lasers in Engineering* **50**, (12), 2012 (1740–1745).

43. A. M. Brittan, "The Study of Mechanical Properties of Welded and Base Material after Exposure to Supercritical CO2," University of Wisconsin-Madison, 2018.
44. A. M. Brittan, J. T. Mahaffey, N. E. Colgan, M. Elbakhshwan, and M. H. Anderson, *Corrosion Science* **169**, 2020 (108639).
45. J. K. L. Lai, *Materials Science and Engineering* **61**, (2), 1983 (101–109).
46. "Boiler and Pressure Vessel Code: Section III Division 5." The American Society of Mechanical Engineers, New York, 2019.